ICAS-98-7,9,3

RELIABILITY EVALUATION OF AEROSPACE COMPONENTS

Saša Jeremić, MSc, Aleksandar Bengin, MSc

Institute of Aeronautics, Aeronautical Engineering Department
Faculty of Mechanical Engineering, University of Belgrade
27. marta St. 80,
11 000 Belgrade, F.R. of YUGOSLAVIA

Abstract

This paper presents analytical and numerical model of flow through two-dimensional rotor cascade, solved by linear vortex panel method. Basic mathematical model is applied on real rotor blade cascade with designed airfoil. Simulation of uncertainties of random variables, that influence structural analysis and design, is based on finite element method. It was simulated static, dynamic and fatigue response of turbine blade. Sensitivity of random variables uncertainties is quantified by the sensitivity factor, useful in design, control and maintenance, as well as in meeting safety requirements. Life of turbine blades and risk associated with reusage of the blade, are calculated. For this purpose, it is introduced methodology of analysis of structure submitted to the stochastic loads, and calculated density distribution function for the first phase of system degradation. Also, it is presented statistical simulation of no balanced low pressure rotor blades, based on lows of statistics and probability. Importance of uncertainty of load function is successfully identified in the analysis of non balanced rotor. This methodology can be used for more complex components and systems in determination of reliability, safe life and associated risk. It, also, can be implemented in the definition of certification procedure, number of tests, criteria and control intervals, as well as in maintenance procedure.

1. Introduction

In this paper straight cascades are considered. This model is a simplified approximation of axial turbine cascades, which are the result of a more contemporary approach, compared with the centrifugal concepts. The results that are presented are obtained for the cases of steady, inviscid, incompressible 2D fluid flow over simulated rotor airfoil-cascades by the vortex lattice method. The computer program is applied for the case of the low-pressure turbine, by application of particular program modules. Theoretical rotor blade shape is on ***CDC Cyber 910*** work-station applying the ***ICEM DDN*** software. All data are stored in data bases, which are later used for aerodynamic and structural analyses. For further graphic applications, the ***AutoCAD*** package is used, while structural analyses are done by application of ***ALGOR*** software.

2. Analysis of the Aerodynamic Characteristics

2.1 Analytical Model of the Airflow

The inviscid irrotational flow is considered, so the existence of the velocity potential can be assumed. In that case, the continuity equation can be reduced to the equation of Laplace, i.e. $\Delta\varphi = 0$. For 2D case, it has the form:

$$\frac{\partial^2\varphi}{\partial x^2} + \frac{\partial^2\varphi}{\partial y^2} = 0 \qquad (2.1)$$

where $\partial\varphi/\partial x = u$ and $\partial\varphi/\partial y = v$; u and v are velocity components in x and y direction. The boundary condition is:

$$\left(\vec{V}_a - \vec{V}_T\right)\cdot\vec{n} = 0 \qquad (2.2)$$

in which $\vec{V}_a$ is absolute velocity, $\vec{V}_T$ is transition velocity, and $\vec{V}_a - \vec{V}_T$ is the relative velocity with respect to the coordinate axes connected to the cascade airfoil, while $\vec{n}$ is the normal vector at any arbitrary airfoil point. In order to obtain a unique solution of the velocity potential equation, it is necessary and sufficient to add the ***Kutta*** condition, which specifies the circulation around the airfoil. For a steady case, it can be expressed by the trailing edge vorticity condition as:

$$\gamma_{ii} = 0. \qquad (2.3)$$

One of the singular solutions of (2.1) is a discrete, isolated vortex of magnitude Γ. By the superposition of uniform, inviscid and incompressible flow and the vortex-induced flow, the curved streamlines are obtained. So the potential flow with circulation is generated, in which the flow is irrotational in the whole flowfield, except generally speaking, in singular points defined by vortices.

Vortex in (x_v, y_v) induces in an arbitrary point (x, y) velocity components u and v:

$$u = \Gamma U_i(x, y, x_v, y_v), \quad v = \Gamma V_i(x, y, x_v, y_v) \qquad (2.4)$$

where U_i and V_i are the velocity components induced by the unit $(\Gamma = 1)$ ith isolated vortex. Vortices are distributed on the panels along the cascade airfoil contours. Thus each vortex belongs to the vortex cascade, tilted at an angle β with respect to the x – axis of the

21st ICAS Congress
13-18 September 1998
Melbourne, Australia

adjacent coordinate system. The cascade pitch is t (see Fig. 1). The arbitrary cascade vortex is defined by coordinates (x_o, y_o).

By similar reasoning, induced velocities in (x, y) by vortex cascade (which is also a singular solution of 2.1) can be calculated by:

$$u = \Gamma U_c(x, y, x_o, y_o, \beta, t),$$
$$v = \Gamma V_c(x, y, x_o, y_o, \beta, t) \qquad (2.5)$$

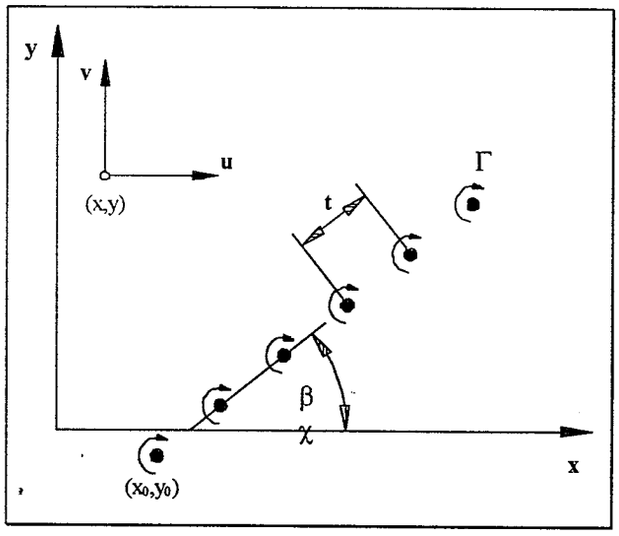

FIGURE 1 - Vortex cascade at angle

Differential equation (2.1) is linear and permits the superposition of solutions, either those given by equations (2.4) or by equations (2.5). It comes from the known fact that any linear combination of singular solutions of (2.1) is also a solution of this equation, by which the specified boundary conditions can be satisfied.

2.2 Numerical Flow Modelling

Reduction of the realistic 3D flow to the plane 2D flow through the cascade is done by introducing simplifications to the real life model. The most significant difference is the mutual interference of the constantly spaced airfoils of the plane model, and the variable density of the blades with respect to the local radius and blade height (h). that difference becomes less significant at high ratio h/l. Also, in real life, streamlines do not follow the blade contours at constant radial distributions due to the existence of radial velocity component. Again, if h/l is high enough, radial velocity components are small enough, and 2D simplification can be quite reasonable.

Discrete vortices can be continually distributed along a plane segment, as shown in Fig. 2. The vortex intensity of the length $d\ell$ is $d\Gamma = \gamma \cdot d\ell$, where γ is vorticity or circulation along the unit length.

If we denote the vorticity γ at the first point of the vortex panel by γ_1 and at the last panel point by γ_2, and if their

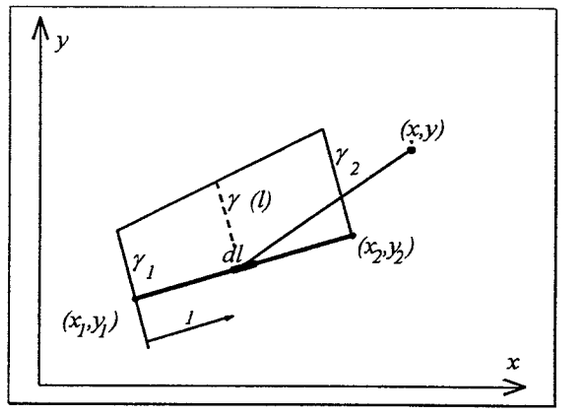

FIGURE 2 – Linear vortex panel

coordinates are (x_1, y_1) and (x_2, y_2) respectively, the induced velocities at an arbitrary point (x, y) can be determined by integration along the segment length:

$$u = \int_0^L \gamma(\ell) U_i(\ell) d\ell \qquad v = \int_0^L \gamma(\ell) V_i(\ell) d\ell \qquad (2.6)$$

in which $U_i(\ell)$ and $V_i(\ell)$ are the velocities induced in arbitrary point by an isolated unit vortex at the position ℓ on the panel. Integration is performed along ℓ so that x and y are integration parameters. Similar equations exists for the cascade panels:

$$u = \int_0^L \gamma(\ell) U_c(\ell) d\ell \qquad v = \int_0^L \gamma(\ell) V_c(\ell) d\ell \qquad (2.7)$$

where U_c and V_c are velocities induced by cascade of unit vortices, at the position ℓ at the panels. The first coordinate (x_1, y_1), the last coordinate (x_2, y_2) of the segment, angle β and the distance between vortices are the integration parameters. While the integral for the isolated panel can be solved analytically, for the panel cascade, no analytical solution for induced velocity exists. It can only be obtained numerically, and one of the possible ways is the application of the ***Gauss-Legendre*** integration formula, involving analytical relations for an isolated panel:

$$u = N\int_0^L \gamma(\ell)\left[U_c(\ell) - U_i(\ell)\right]d\ell + \int_0^L \gamma(\ell) U_i(\ell) d\ell$$
$$v = N\int_0^L \gamma(\ell)\left[V_c(\ell) - V_i(\ell)\right]d\ell + \int_0^L \gamma(\ell) V_i(\ell) d\ell \qquad (2.8)$$

where N denotes the integrals that should be calculated numerically. By this, numerical calculation of induced velocities at the control points of the panels by which airfoil contours are approximated is avoided, since the numerical error of such procedure would be very significant.

Figure 3 shows the trailing edge approximated by linear segments. Nodes (dark circles) represent the boundaries of segments, while transparent circles represent control points. The number of the control point is also the number of the segment. There is one control point less than the number of the unknown vorticities. Two adjacent segments $i-1$ and i share the common point i where the unknown vorticity γ_i is placed.

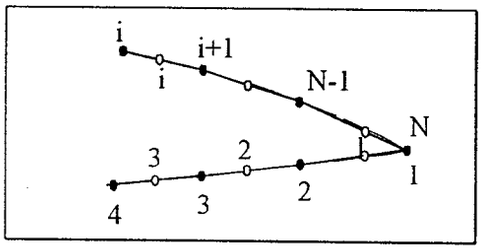

FIGURE 3 – Airfoil approximated by panels

At each control point ν the boundary condition (2.2) should be satisfied (here $U_T = 0$ and $\omega = 0$, while $_T$ is tangential velocity due to the rotation of the rotor cascade:

$$\sum_{i=1}^{j=N}(u_{\nu,i} - y'_\nu v_{\nu,i} - \Delta\ell_i/2t)\gamma_i = (V_n\cos\alpha_n - \\ - U_T + \omega y_\nu)y'_\nu - V_n\sin\alpha_n + V_T + \omega x_\nu \tag{2.9}$$

in which $u_{\nu,i}$ and $v_{\nu,i}$ are the velocities induced in ν due to the unit vorticity of the vortex i, and $\Delta\ell_i$ is a part of the segment length that corresponds to the unknown vorticity γ_i. The summing is done for all N unknowns. The number of control points ν on airfoil for one lower than the number of unknowns. The supplementary equation for the Nth unknown is determined from the ***Kutta*** condition, by which the finite velocity value is obtained at the trailing edge. That condition is numerically given by:

$$\gamma_1 + \gamma_N = 0 \tag{2.10}$$

Thus a set of N equations with N unknowns is obtained.

$$\begin{bmatrix}[A]\\ [101]\end{bmatrix}_{N\times N} \times \begin{Bmatrix}\gamma_i\\ \gamma_N\end{Bmatrix}_N = \begin{Bmatrix}R\\ 0\end{Bmatrix}_N \tag{2.11}$$

2.3 Calculation Procedure and Results

Elements of the matrix [A], which is of the order *(N-1)xN* are the aerodynamic influence coefficients $a_{\nu,i} = v_{\nu,i} - y'_\nu u_{\nu,i} - \Delta l_i/2t$ (see equations 2.10). At the same time matrix [A] is the matrix of self-induction, i.e. it contains cascade panel vortex influences on the control points of the airfoils of the same cascade. Matrix of the type [101] and order *1xN* defines the ***Kutta*** condition at the trailing edge. Vector $\{\gamma_i\}$, which is of the order *(N-1)x1*, contains the unknown vorticities. Elements of the vector $\{R\}$, which is of the order *(N-1)x1)* are $r_\nu = y'_\nu V_n\cos\alpha_n + V_T - V_n\cos\alpha_n$ since $U_T = \omega = 0$; for the rotor we have $V_T \neq 0$.

First the coordinates of nodes, coordinates and slopes of control points and lengths of corresponding panels should be determined. After that coefficients $a_{\nu,i}$ and elements $r_{\nu,i}$ (for given V_n, α_n, V_T) are calculated and substituted in the matrix equation (2.11). All unknown values γ at nodes are obtained as solutions of that equation.

Now the circulations around airfoils are now obtained:

$$\Gamma = \sum_1^N \Delta l_i \gamma_i \tag{2.12}$$

as well as the velocities in control points ν:

$$U_{\tau\nu} = V_n\cos\alpha_n + \omega_{x_\nu}$$
$$V_{\tau\nu} = V_n\sin\alpha_n + \omega_{y_\nu} - V_T - \Gamma/2t \tag{2.13}$$

Then pressure coefficient and aerodynamic coefficients (as functions of the on-coming stream velocity) acting on a cascade airfoil can be calculated as:

$$C_{P\nu} = 1 - \left(U_{\tau\nu}^2 + V_{\tau\nu}^2\right)/V_n^2$$
$$C_y = \frac{1}{l}\sum_{\nu=i=1}^{N-1} C_{P\nu}\left(x_{i+1} - x_i\right)$$
$$C_x = \frac{1}{l}\sum_{\nu=i=1}^{N-1} C_{P\nu}\left(y_{i+1} - y_i\right) \tag{2.14}$$
$$|C_n| = \sqrt{C_y^2 + C_x^2}$$

where $x_i, x_{i+1}, y_i, y_{i+1}$ are coordinates of panel nodes to which a particular control point belongs, and l is the chord of cascade.

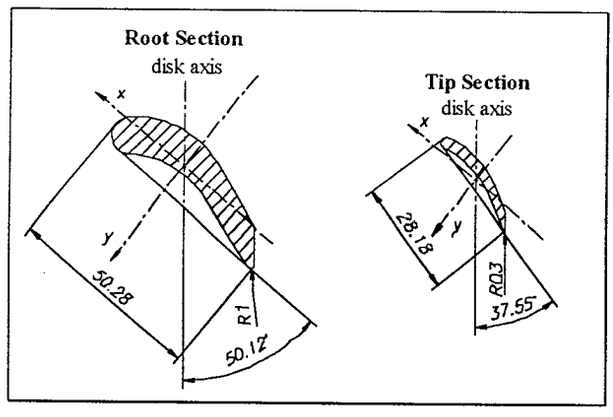

FIGURE 4 – Blade airfoils

Based on the presented theory, a computer program for flow calculation has been developed. Calculations were done for a rotor cascade with 50 control points on each

airfoil, by which a sufficient numerical accuracy has been achieved (curves of Cp distribution are smooth).

In Fig. 5 Cp distribution is presented as a function of the on-coming flow velocity V_n (which slightly differs from the values that are obtained when instead of V_n, free-stream velocity V_∞ is used.

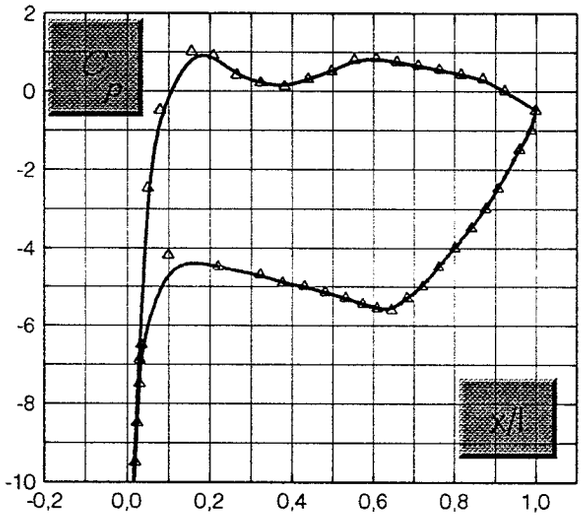

(a)

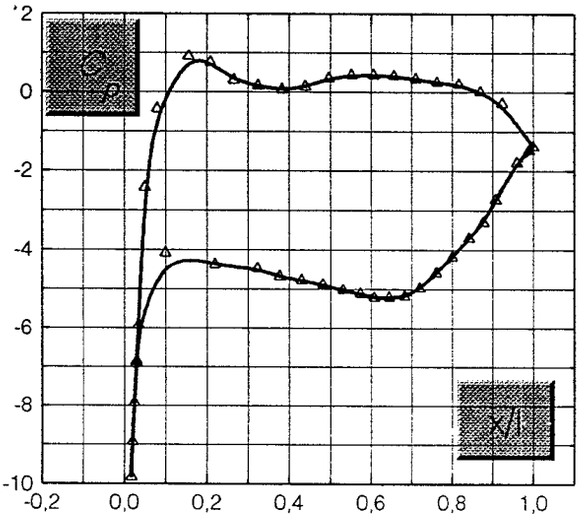

(b)

FIGURE 5 – Chordwise distribution of pressure coefficient Cp, (α= 20^0): (a) root section; (b) tip section

3. Structural Analysis

Structural components in mechanical and aeronautical systems are generally subjected to a variety of complex, severe cyclic and transient loading conditions, including high temperatures and steep temperature gradients. Most of these conditions introduce uncertainties which are quantifiable only as best engineering estimates. These complex loading conditions subject the material to coupled non-linear behaviour which depends on stress, temperature and time. Coupled non-linear material behaviour is nonunifom, very difficult to determine experimentally, and perhaps impossible to describe deterministically.

The aim of this paper was to further improve the structural analysis, initially done by ***ALGOR*** software, by introducing computer simulations based on the known probabilistic theories and statistics. Examples of material behaviour and structural analysis of turbine blade, as well as of complete unbalanced rotor will be given.

3.1 H-adaptive Finite Element Procedure

Finite element analysis is done on H-adaptive grid. In order to perform this kind of calculation, it is necessary to define and evaluate errors in the calculation domain, which will enable us to define necessary grid densities in certain areas and so improve complete calculation accuracy.

The error evaluation implies that C^o displacement continuity in nodes and at the element boundaries is satisfied (for 2D finite element problems), or C^1 continuity (for 3D problems of plates and shells bending).

While calculating stress and strain fields, at the element boundaries the discontinuities appear. That practically means that at a certain point of continuum (approximated by finite elements) using standard finite element methods, stress and strain can not be uniquely solved. This problem can be solved by application of the smoothing method.

Generally, relative stress error η_{perm}(in %) should be predefined (in case of some commercial softwares it is approximately 5%), so that after the final analysis the following should be satisfied:

$$\eta \leq \eta_{perm}. \qquad (3.1)$$

The value ξ_i defines the subdomain coyered by element i at which it is necessary to increase finite element grid density (if $\xi_i > 1$) or decrease it (if $\xi_i < 1$).

If the finite element i is of the size h_i, and p is the highest order of the interpolation polynomial function, than the dimensions of new finite elements are:

$$h_{inew} = \frac{h_i}{\xi_i^{1/p}} \qquad (3.2)$$

This means that, if errors are not evenly distributed, (which is almost always the case in the first iteration), for the second iteration step finite element grids are generated by assumed element dimensions.

Equation (3.2) is the basic equation for H-adaptive finite element grid. In practical applications, one or two iterations are sufficient for obtaining the "optimal" grid.

Value ξ_i can be calculated as a ratio:

$$\xi_i = \frac{\Delta\sigma}{\sigma_{perm}} \tag{3.3}$$

where:

- $\Delta\sigma$ is the stress "jump" (in case of unsmoothed values) between the two adjacent elements,
- σ_{perm} - predefined allowed stress "jump", for instance as 5% value of the highest stress appearing in the structure, while it should be satisfied that $\eta \le 5\%$.

Application of the adaptive finite element grids eliminates experience as a key factor for obtaining correct results. That actually means that first, i.e. initial finite element grid can be created arbitrarily. The only condition that should be satisfied is that any physical domain must be represented by at least two finite elements. If that is not satisfied, there is no way to perform the smoothing of the results, or to calculate the error in the energetic form, since there are no stress discontinuities. Further grid generation through prescribing η_{perm} and σ_{perm} is done automatically. By this very accurate data concerning geometric factors of stress concentration are obtained.

3.2 Probabilistic Material Behavior Model

Due to variations in the manufacturing process, the microstructure of a material is never uniform. This nonuniformity results in the uncertainty of material properties. Also, it has been shown that material properties degrade according to the type and history of loads the material experiences. Loads also have uncertainties of their own. Therefore, it is important to quantify the uncertainties in the material properties using probabilistic methods.

A generic material behaviour model called the multi-factor interaction equation *(MFIE)* model. The fundamental assumption for this model is that material behaviour can be simulated by primitive variables. The general form of this model is given by:

$$\frac{M_p}{M_{po}} = \left(\frac{T_F - T}{T_F - T_o}\right)^n \left(\frac{S_F - \sigma}{S_F - \sigma_o}\right)^p \left(\frac{\log N_{MF} - \log N_M}{\log N_{MF} - \log N_{M\,o}}\right)^q$$

where subscript ***P*** denotes the material property, the subscript ***F*** denotes the condition at the final stage, and the subscript ***o*** denotes the condition at the reference stage. The exponents ***n, p,*** and ***q*** are determined from the available experimental data or estimated from the anticipated material behaviour due to a particular primitive variable. Each term in parentheses is called an ***effect***. Any number of effects can be included in the equation. In general, the generic form of the equation is:

$$\frac{M_P}{M_{PO}} = \prod_{i=1}^{N} \left[\frac{(V_F - V)}{(V_F - V_O)}\right]_i^a \tag{3.5}$$

Each primitive variable V for a material and exponent a in the above equation can be random with any statistical distribution. The inadequacy of a set of experimental data can be taken into account by means of the uncertainties in the exponent. The ***MFIE*** model to perform probabilistic simulation of material behaviour and evaluations of subsequent structural responses.

3.2 Model and Temperature and Pressure Distributions

The mean temperature and pressure distributions are shown in Figs.6 and 7, respectively. It is assumed that all random fields were independent of each other. However, the correlation coefficient between random variables in the same field was defined as:

$$\rho(X_i, X_j) = e^{(-\Delta X_{ij}/S_c)} \tag{3.6}$$

where X_i and X_j were the *i*th and *j*th random variables in the *X*-coordinate random field; ΔX_{ij} was the distance between X_i and X_j. S_C was the correlation length.

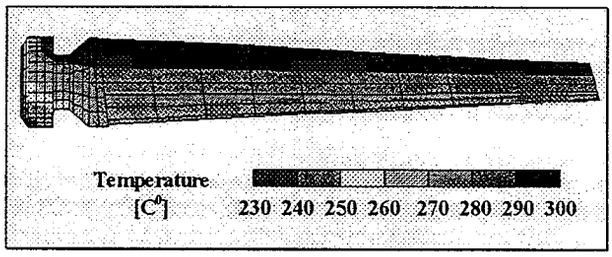

FIGURE 6 – Steady-state temperature distribution

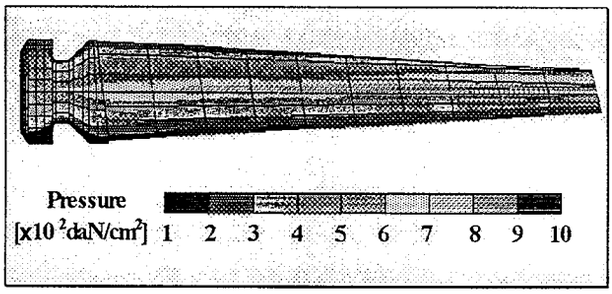

FIGURE 7 - Steady-state pressure distribution

The greater the correlation length, the greater the correlation between the random variables in a random field. When S_C was extremely large, the random field could be represented by a single random variable. When S_C approached zero, the random variables were uncorrelated. Each correlated random field was decomposed into functions of independent random variables. The blade was modeled by 170 four-node elements. The blade was assumed to be fixed at the root.

3.3 Response Analysis

The blade responses analyzed were the effective stress.

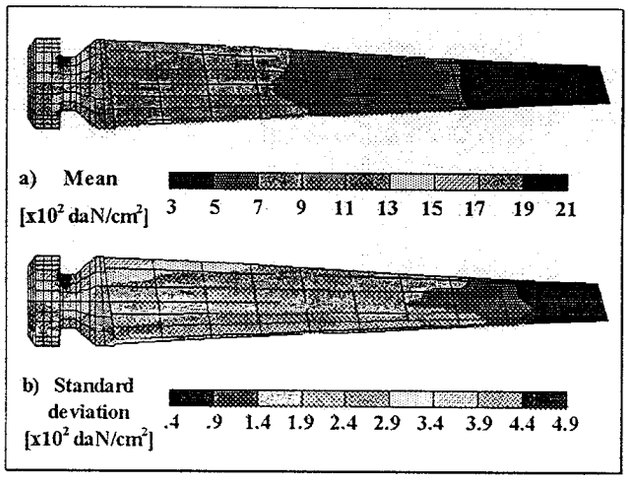

FIGURE 8 – Effective stress on pressure side

The mean, standard deviation, and coefficient of variation of the effective stress, which appears due to aerodynamic loading, is shown on Fig.8. The highest mean effective stress was 2100 dan/cm^2 at the lower corner of the leading edge. The coefficient of variation associated with this critical stress was 3%. Based on this information, a blade risk analysis was performed. The failure mode was defined as the case where the stress value exceeded the material strength. The probability of failure was calculated by:

$$P_f(i) = \int f_{\sigma_i}(X) F_{S_i}(X)\, dX \qquad (3.7)$$

where f_σ was the probability density function of effective stress at the ith node. F_S was the density function of strength at the ith node, which was normally distributed with a mean of 2100 dan/cm^2 and standard deviation of 290 dan/cm^2.

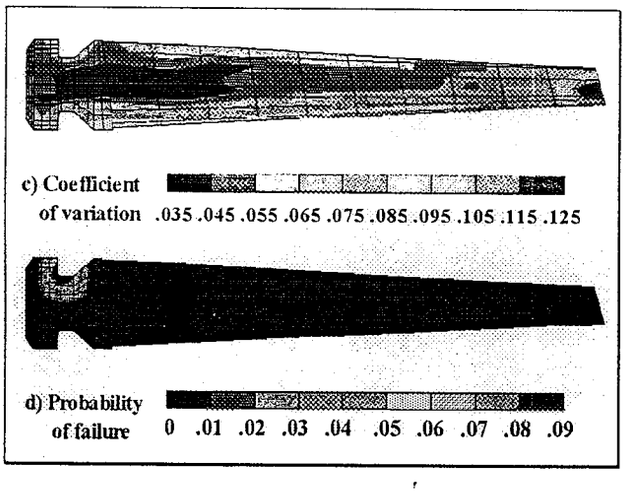

FIGURE 8 (continued) - Effective stress on pressure side

The failure probability at each nodal point was obtained and is shown in Fig.8(d). As was expected, the location of highest failure probability was the lower left corner (at the root of the blade leading edge).

Sensitivities of the independent random variables to the probability distribution for any response were also computed. This sensitivity information, quantified by sensitivity factors, was used to define the role of the random variables in the reliability analysis. Sensitivity factors indicate which random variables are crucial and will therefore require more attention both during the manufacturing process and while experiencing environmental conditions (i.e., loading, temperature).

The sensitivity factors for the effective stress at the airfoil leading-edge root were obtained. The five most influential random variables related to the Z-coordinate, elastic modulus, and rotational speed are listed in Table 1. As expected, the temperature random field had an insignificant effect on the stress value. The Z-coordinate random field was found to be crucial. The rotational speed, which induces centrifugal forces, was another important random variable. The uncertainties of the effective stress at a root can be minimised significantly if the uncertainties of those five random variables are reduced. This information can help an engineer to efficiently improve the design and reliability of a blade.

Table 1. *Five independent random variables most influential to the effective stress at root*

Random fields	nth independent random variable in each field	Sensitivity factor	Ranking
Z coordinate	1	0.252	4
Z coordinate	2	0.631	1
Z coordinate	4	0.289	3
Elastic modulus	10	0.196	5
Rotational speed	1	0.332	2

3.4 Probabilistic Fatigue/Damage Analysis

Reliability and durability assessment are essential for component certification. Components subjected to cyclic loads ultimately become damaged and continue to accumulate damage due to material property/strength degradation. A sample methodology for the probabilistic assessment of the life of and risk associated with components turbine blade model will be given. The method involves a probabilistic damage analysis for

damage initiation, damage propagation, and determination of the most damage path.

Material property/strength degradation due to cyclic loading on the turbine blade was simulated using the multi-factor interaction equation model (see Eq.(3.4)).

The simulation was done in several steps:

1.) Since the stress magnitudes were unknown, the initial probability distributions of the material properties were predicted using reference values and the temperature field for a given fatigue life;

2.) The probability distributions of stresses were computed;

3.) The joint probability distribution of the stress field was calculated using:

$$P(\sigma_i \le y_i \wedge \sigma_j \le y_j) = \Phi(-B_i)\Phi(-B_j) + \int_0^{p_{ij}} \Phi(-B_i, -B_j, z)dz \qquad (3.8)$$

where p_{ij} was defined by $p_{ij} = \sum_{k=1}^{n} \alpha_{ik}\alpha_{jk}$ and were α_{ik} was the kth sensitivity factor, n was the number of random variables, and B_i was the reliability index;

4.) Using the distributions obtained in steps 2 and 3, the probability distributions of material properties for a given fatigue cycle were obtained over the entire component;

5.) Steps 2, 3 and 4 were repeated until the probability distributions of stresses and material properties over the entire model converged.

Damage initiation occurs when the stress is greater than the strength. The following steps were used to obtain the ***risk/fatigue*** cycle curve:

1.) For a given fatigue cycle, the probability distribution of effective stress f_σ was obtained using the steps described earlier for probabilistic fatigue life analysis;

2.) Using the probability distributions of stress and strength (f_σ and f_S, respectively) for a given fatigue cycle, the probability of damage initiation p_f was calculated using:

$$p_f = \int_{-\infty}^{\infty} \left[\int_{-\infty}^{x} F_s(s)ds \right] f_\sigma(x)dx \qquad (3.9)$$

3.) Steps 1 and 2 were repeated to obtain risk/fatigue cycle curves for critical locations and different cycles.

The blade was assumed to be subjected to a given number of fatigue cycles which degraded the modulus of elasticity, thermal expansion coefficient, and material strength. Damage initiation occurred when the stress exceeded the strength. The critical points A and B (see Fig.10) experiencing large displacement and high stress. At the root of the leading edge, the probability distribution of the modulus elasticity was reduced significantly following application of cyclic loads.

By varying the number of cycles and repeating the overall procedure described previously, a ***risk/fatigue*** cycle curve was developed for critical locations (see Fig.9). Such a curve is useful for assessing the structural risk due to fatigue. For instance, at a given acceptable risk level, the number, of fatigue cycles required to initiate local damage can be determined. With this information available, criteria can be set for quality control, inspection intervals, and retirement-for-cause.

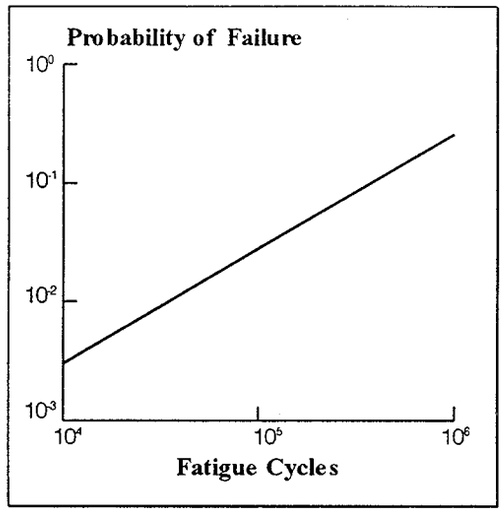

FIGURE 9 *– Probability of local failure at node A due to fatigue cycles*

It is often important to know whether a structure will operate safely or will experience significant cleavage or ductile damage when a damage site has just initiated. Such a situation can be quantified probabilistically by determining the most probable damage initiation site, the most probable damage growth path, and the corresponding structural integrity degradation due to damage growth and loading history.

The probable damage path can be determined as follows: Let S^0 represent the structure in its undamaged state (i.e., with no pre-existing damage) and S^{ijk} represent a damaged state in which damage has occurred consecutively at nodes ***i, j,*** and ***k***. Let node ***l*** represent the node that will next experience damage when the structure is in the damaged state S^{ijk}. The state indicating the collapse of the structure is called the terminal state. This state occurs when the probability of collapse is equal to 1.0 and the strain energy has a sudden jump. Let S^{ijk} be the terminal state. The probability of reaching the terminal state is the probability that events M_i^0, M_j^i, and M_k^{ij} will all occur, which is given by:

JEREMIĆ

$$P(\text{damage path through nodes } i,j,k \text{ occurs}) = P\left(M_i^0 \cap M_j^i \cap M_k^{ij}\right) \quad (3.10)$$

where $\cap$ denotes the intersection of probability events.

There were many possible damage paths for the model. The two most probable are shown in Fig.10 as path 1 and 2. For path 2, the first damage location was at node A, with a probability of damage initiation equal to 0.10. At damaged state S^A, the probability of advancing the damage to node E was 0.0002. When both nodes A and E were damaged, the probability that node C would be damaged next was 1.0. The change of mean strain energy going from damage state $S^{A,E}$ to $S^{A,E,C}$ was small. However, when the damage extended to node D, the mean strain energy had a sudden jump, indicating that global structural failure was imminent. Therefore, $S^{A,E,C}$ represented the terminal state.

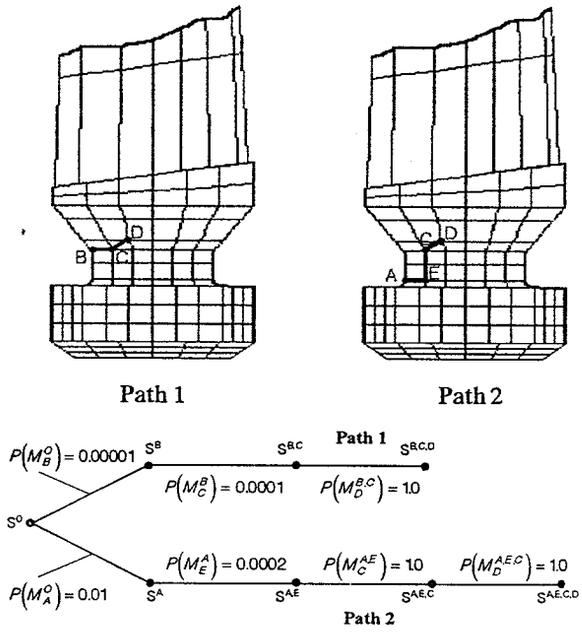

***FIGURE 10** - Most probable damage path caused by 10^5 cycles, where S indicates damage states at various nodes and P(M) indicates the probability that the next damage event will occur at a particular node*

Using Eq.(3.10), the probability of occurrence for path 2 was determined by:

$$P(\text{path 2 occurs}) = P\left(M_A^0 \cap M_E^A \cap M_C^{A,E}\right) \quad (3.11)$$

Similarly, the probability of occurrence for path 1 was given by:

$$P(\text{path 1 occurs}) = P\left(M_B^0 \cap M_C^B \cap M_D^{B,C}\right) \quad (3.12)$$

The probability of occurrence for path 2 was 20 times greater than that for path 1. Therefore, path 2 was the most probable damage path.

Structural components that either contain damage initially or develop damage early in their lives may still carry their service loads safely, however. Practical limitations in manufacturing and inspection and the use of many structural components in a system prohibit complete elimination of flaws. In cases where these initial flaws are present, the period of propagating damage may occupy a significant portion of the usable component lifetime. Therefore, the determination of damage propagation due to cyclic load is essential for setting guidelines for inspection intervals and retirement-for-cause. Inspections should be conducted to detect and repair defects prior to the onset of global damage.

The fundamental failure mechanism by which damage may propagate occurs when the load effect is greater than the material resistance at the current structural conditions. The undamaged state may be defined as the state where the risk or the probability of damage initiation is less than the maximum allowable value. As the number of load cycles increases, the material properties and strength degrade, the stress distribution changes, and the risk level reaches its maximum allowable value. At this point, a new damage mechanism forms. The damage is either initiated or is advanced, and a reliability assessment of fatigue life is needed to provide a basis for ensuring safe operation.

A probabilistic structural life can be divided into two periods, initiation life and propagation life, for a given risk level. The risk level is based on the cost of upgrading the material and on the cost of the consequences of structural failure.

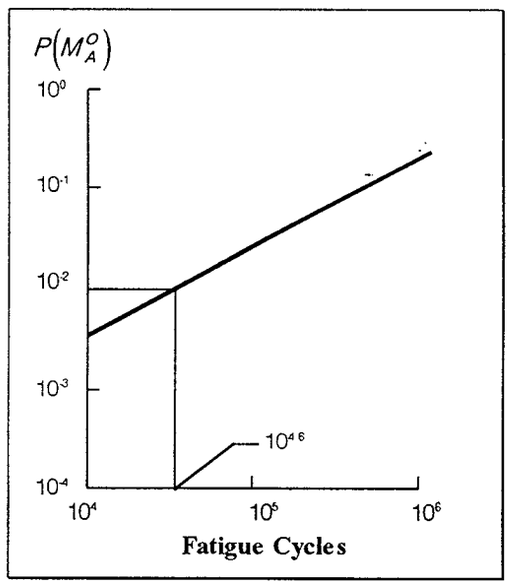

***FIGURE 11** – Probability of crack initiation at node A at damaged state S^O [or $P(M_A^O)$]*

During its initiation life, as shown in Fig.11, the probability of damage initiation at nodal point A was lower than the maximum allowable risk for a number of

fatigue cycles less than $10^{4.6}$. Once the number of cycles exceeded this value, damage was assumed to have occurred. A probabilistic structural analysis was performed for this damaged structure and this number of fatigue cycles. The location with highest probability of failure (node E) was detected, and the structure underwent damage propagation.

The probability of forming a new failure mechanism was smaller then that for the maximum allowable risk et the beginning of the propagation life (see Fig.12). The structure was deemed safe and able to resist additional cycles. When the number of cycles increased, such material properties as modulus of elasticity, strength, and damage toughness were degraded according to Eq.3.4. At $10^{5.6}$ cycles, the maximum allowable risk level was reached, and the damage advanced from node A to node E. The damage propagation rate was determined as:

$$\frac{da}{dN} = \frac{a(E,A)}{10^{5.6} - 10^{4.6}} = 4.2 \times 10^{-6} \frac{cm}{cycle} \qquad (3.13)$$

where N was the number of cycles and ***a(E,A)*** the distance between nodes E and A.

This procedure was repeated while increasing the number of cycles until the risk rapidly surpassed the allowable bounds for damage propagation to node C (see Fig.13). Prior to this number of cycles ($10^{5.6}$ cycles), the structure would have had to be retired-for-cause due to global structure damage.

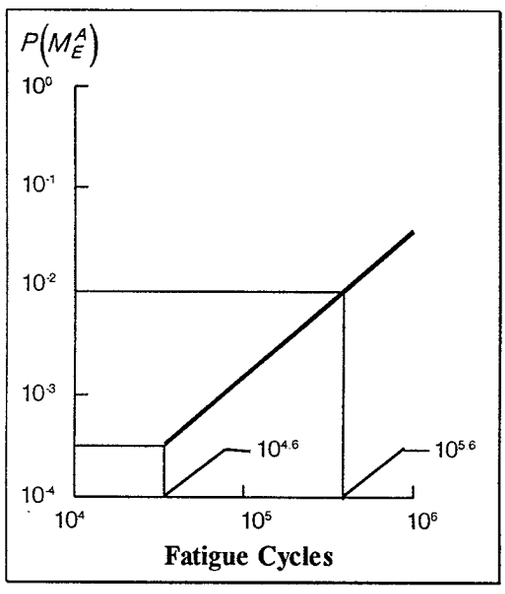

FIGURE 12 – Probability of crack being extended to node E at damaged state S^A [or $P(M_E^A)$]

For this blade, the inspection intervals could be set during the damage propagation process to ensure safety. For example, if the maximum allowable probability of failure was set at 10^{-3}, the structure would be inspected right after 10^5 cycles.

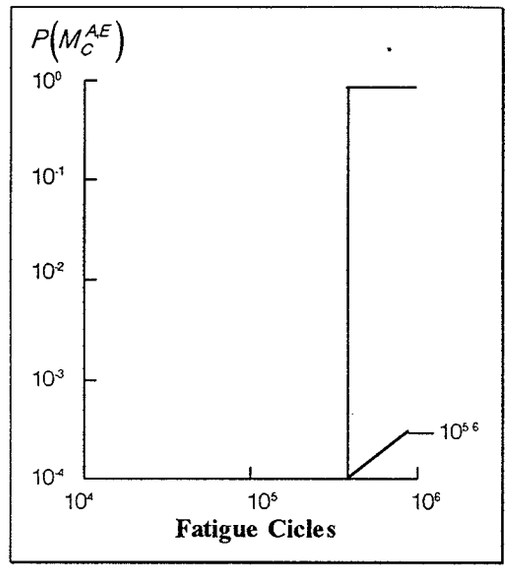

FIGURE 13 - Probability of crack being extended to node C at damaged state $S^{A,E}$ [or $P(M_C^{A,E})$]

4.0 Adjusting of Bladed Disks

Inherent uncertainties in blade geometry, material properties, damping, mass, etc., results in uncertainties of dynamic characteristics. Because of these uncertainties, each blade on a rotor disk does not have the same fundamental frequency. These differences are referred to as mistuning. When blades with such small variations in frequencies operate together on a rotor disk, their individual amplitudes and dynamic stresses are altered significantly. This alteration is the effect of mistuning. The overall disk assembly will have many vibration modes very close to one another, resulting in a significant amplification of the responses. To evaluate the scatter in the amplified responses, it is important to account for the uncertainties that contribute to the blade response amplifications. In this study, both structural and load uncertainties were included to quantify the amplified response uncertainties by performing probabilistic forced dynamic response.

The governing equation of motion for the bladed disk was given by:

$$[M]\{\ddot{X}\} + [C]\{\dot{X}\} + [K]\{X\} = \{A e^{i(\Omega t - \Psi)}\} \qquad (4.1)$$

where $\ddot{X}$, $\dot{X}$, and X were the acceleration, velocity, and displacement, respectively.

A lumped mass-spring model representing the blades and rotor disk, as shown in Fig.14, was used for the analysis. The disk was represented by lumped masses connected by a set of radial and circumferantial springs. The masses representing the blades were mounted on each disk mass.

JEREMIC

Each blade was modelled by two lumped masses, one corresponding to the airfoil region and the other to the shank and fir-tree region. The lumped masses were connected by beam elements. The radial and circumferantial beam elements for the disk had only extensional stiffness representing the respective stiffness for the disk. The beam elements connecting the blade masses had only bending stiffness to account for the flexural mode of vibration of the blade. Therefore, it is important to note that only the bending mode of vibration for the blade was considered in the analysis since such vibration normally dominates the responses. Thus, the dynamic interaction between the blades came through disk springs and masses.

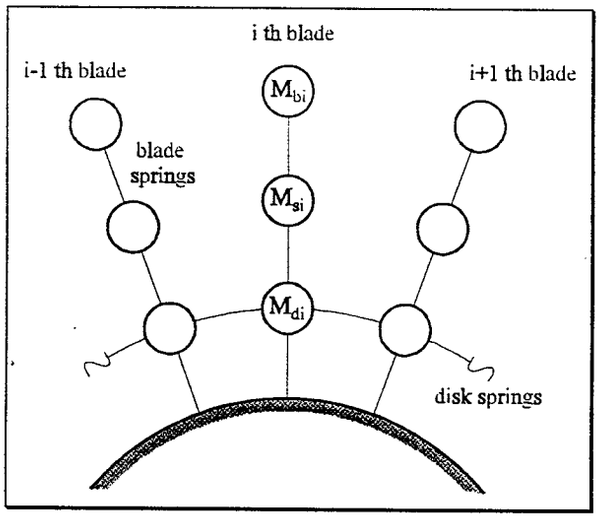

FIGURE 14 – Lumped mass-spring model for bladed disk

4.1 Loads

Forces induced on blades are due to variations in the flow in a circumferantial direction. The variations the flow are considered to be periodic in nature. Therefore, the excitation is harmonic, which is characterised by amplitude, frequency of excitation, and phase angle. The magnitude of the amplitude does not matter in the case of linear analysis, since an assessment is based on responses normalised to those of a tuned rotor. However, the statistical distribution of the amplitude does matter.

A tuned rotor is one for which all the individual blade frequencies are the same. The frequency of excitation selected is an integer multiple of the engine rpm. The excitation differs from blade to blade only in terms of phase angle. Since the blades are fixed around the circumference, the phase difference is given by:

$$\psi = 2m\left(\frac{\pi}{N_R}\right) \qquad (4.2)$$

where m is the integer multiple between the engine rpm and frequency of excitation, and N_R is the number of blades on the rotor. The modal damping used in this analysis was 5 percent (including material, structural, and aerodynamic damping).

4.2 Results

Normalized amplitude is defined as the ratio of maximum blade response of a mistuned rotor to that of a tuned rotor. The normalized response indicates the amplification of response due to mistuning. Figure 15 shows cumulative distribution function (CDF) of normalized blade amplitude for the rotor with 180 blades.

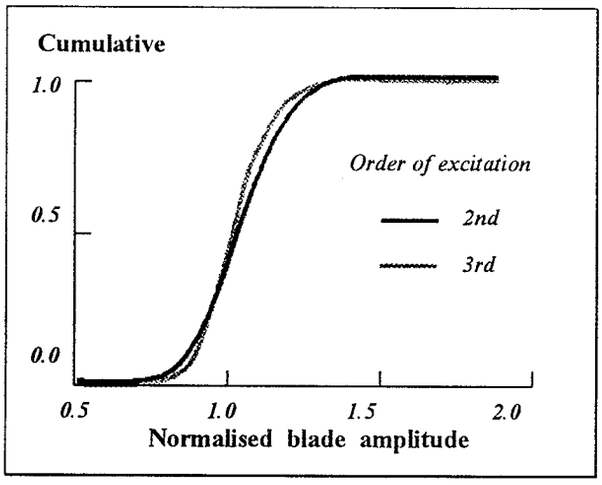

FIGURE 15 - CDF of normalised blade amplitude

As was expected, the results show that, for the same probability level for a given rotor, the amplification of blade response amplitude was higher in the case of second-order excitation, i.e., when the excitation frequency was closer to the natural frequency of a blade. Also, it was observed that for a given order of excitation, the amplification of blade response amplitude increased as the number of blades increased. This increase was due to the fact that as the number of blades on a rotor increases, a higher number of vibration modes get closer to each other.

5.0 Concluding Remarks

Reliability evaluation and calculation in the process of the design of aeronautical components enables obtaining of much more reliable, economical and less costly systems, both from the aspect of production and operation costs. Reliability evaluation, on the other hand, requires large amount of data concerning operating conditions, normal and ultimate loads, as well as their dissipations. Obtaining of these data is generally extremely complicated, since they depend on vast number of factors of statistical nature, and they can be evaluated during many long lasting tests. Here presented algorithms of reliability calculation seem to be costly-effective and rationally applicable for large and expensive production systems. Although, their application should be done with high level of caution in

other cases, since the practice shows that in the design process of certain components, several different experimental and calculation methods and simulation techniques should be tested before optimal one is accepted.

Many structural failures have been attributed to human factors in engineering design, analysis, maintenance, and fabrication processes. The human factor is intertwined among all engineering efforts to develop durable, safe, and reliable products. Every facet of the engineering process (planning, designing, manufacturing, inspection, maintenance, communication, and coordination between engineering disciplines) is heavily governed by human factors and their associated degree of uncertainty.

Many factors – whether societal, physical, professional, or psychological introduce uncertainties that significantly influence the reliability of human performance. Such factors as health, home life, martial status, work load, job satisfaction, and professional status can affect human performance in any engineering activity.

References

[1] Boyce L., Chamis C.C., *Probabilistic Constitutive Relationships for Cyclic Material Strength Models,* 29th Structural Dynamics and Materials Conference, Williamsburgh, VA, 1988.

[2] Shiao M.C., Chamis C.C., *First Passage Problems: A Probabilistic Dynamic Analysis for Degrading Structures,* NASA TM 103755, May 1990.

[3] Shah A., Shiao M., Nagpal N., Chamis C.C., *Probabilistic Evaluation of Uncertainties and Risks in Aerospace Components,* NASA Luis research Center, Ohio 1992.

[4] Shah A., Chamis C.C., *Proceedings of the Structural Integrity and Durability of Reusable Space Propulsion Systems,* Nasa Lewis Research Center, Cleveland, OH, May 1991.

[5] Shah A., Chamis C.C., *Probabilistic Simulation of the Human Factor in Strucrural Reliability,* Nasa Lewis Research Center, Cleveland, 1991.

[6] Jeremić S., Bengin A., Cvetković D., Kostić I., *Spare steam turbine blade designing,* International Congress: "Stvaralaštvo kao uslov privrednog razvoja", Savez inženjera i tehničara Jugoslavije, Belgrade, October 1996.

[7] Khun P., *Stress in Aircraft and Shell Structuress,* Mc Graw-Hill Book Co., New York, 1956.

[9] Jeremić S., *Probabilistic Evaluation of Uncertainties and Risks in Aerospace Components,* MSc Thesis, Faculty of Mechanical Engineering, Belgrade, 1997.

[10] Matejić P., *Analiza koncentracije napona oko otvora tankozidnih struktura,* MSc Thesis, Faculty of Mechanical Engineering, Belgrade, 1996.

[11] Dragović T., Petrović Z., *Numeriçal Estimation of Force Component in the Stator Rotor Cascade,* PICAST2-AAC6, Melburne, Australia, 1995.

[12] Battolle, *Aerospace structural Methods Handbook,* 1985.

[13] Chamis C.C., Rubinstein R., Nagpal V.K., *Probabilistic Structural Analysis to Quantify Uncertainties with Turbopump Blades,* AIAA Journal, Vol.27.No.6, 1989.

[14] Chamis C., Nagpal V.K., Shah A.. *Probabilistic Analysis of Bladed Turbine Disks and the Effect of Mistuning,* NASA TM 102564, April 1990.

[15] Allen D., Haisler W., *Introduction to Aerospace Structural Analisys,* John Wiley & Sons, New York, 1985.

[16] Anderson B., Falk U., Babuska I., von Petersdorff T., *Reliable Stress and Fracture Mechanics Analisys of Complex Components Using a H-P Version of FEM,* International Journal for Numerical Methods in Engineering, Vol.38.,1995.

[17] Alturi S., *Computational Nonlinear Mechanics in Aerospace Engineering,* AIAA,1992.

[18] ALGOR, *Procesor Reference Manual,* Part.442.401, Revision 2, Pittsburgh, April 1992.

[19] ALGOR, *Stress Decoder Reference Manual,* Part.442.401, Revision 2, Pittsburgh, April 1992.

[20] ALGOR, *SuperCap Reference Manual,* Part.442.401, Revision 2, Pittsburgh, April 1992.

[21] ALGOR, *Supergen Reference Manual,* Part.442.401, Revision 2, Pittsburgh, April 1992.

[22] ALGOR, *Supersurf Reference Manual,* Part.442.401, Revision 2, Pittsburgh, April 1992.

[23] ALGOR, *ViziCad Plus Reference Manual,* Part.442.401, Revision 2, Pittsburgh, April 1992.

[24] Bathe K.J., Wilson E.L., *Numerical Methods in Finite Element Method,* Nonlinear Finite Element Analisys in Structural Mechanics, Proceedings of the Europe U.S. Workshop, Rhur-Universitat Bochum, Germany, 1980.

[25] Bathe K.J., *Finite Element Procedures in Engineering Analisys,* Prentice-Hall, Inc., New Jersey, 1984.

[26] Ćirić Lj., *Specialne funkcije,* Faculty of Mechanical Engineering, Belgrade, 1983.

[27] Josifović M., *Izabrana poglavlja iz elastičnosti i plastičnosti,* Belgrade, 1983.

JEREMIĆ